Laplacian Analysis Meets Dynamics Modelling: Gaussian Splatting for 4D Scene Reconstruction

Anonymous authors

Paper under double-blind review

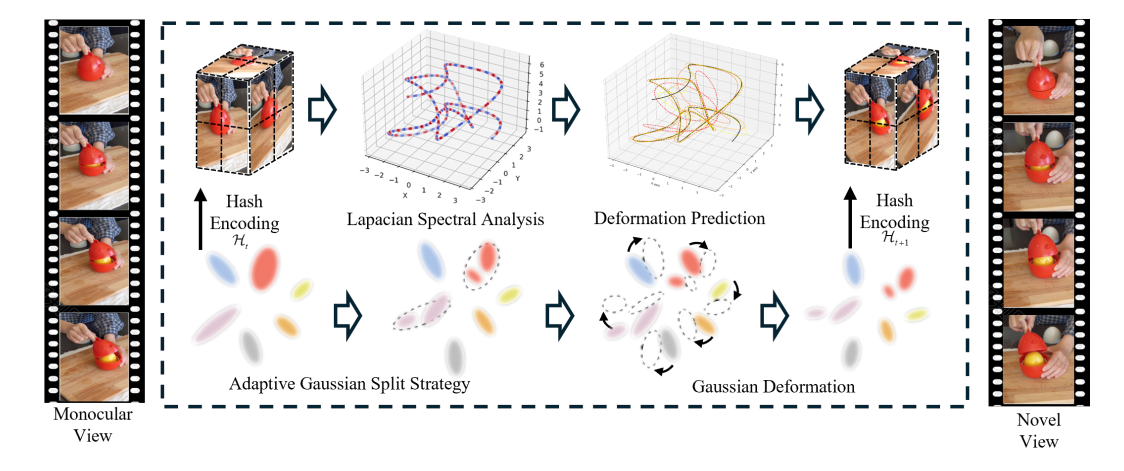


Figure 1: **Overview of our model.** This work integrates Laplacian analysis to model the motion flow more efficiently for 4D Gaussian splatting.

ABSTRACT

While 3D Gaussian Splatting (3DGS) excels in static scene modeling, its extension to dynamic scenes introduces significant challenges. Existing dynamic 3DGS methods suffer from either over-smoothing due to low-rank decomposition or feature collision from high-dimensional grid sampling. This is because of the inherent spectral conflicts between preserving motion details and maintaining deformation consistency at different frequency. To address these challenges, we propose a novel dynamic 3DGS framework with motion flow extraction. Our approach contains three key innovations: a spectral-aware Laplacian motion flow extraction module which merges Hash encoding and Laplacian analysis for flexible frequency motion control, an enhanced Gaussian dynamics attribute that compensates for photometric distortions caused by geometric deformation, and an adaptive Gaussian split strategy guided by KDTree-based primitive control to efficiently query and optimize dynamic areas. Through extensive experiments, our method demonstrates state-of-the-art performance in reconstructing complex dynamic scenes, achieving better reconstruction fidelity and real-time rendering.

1 Introduction

Dynamic scene reconstruction from monocular videos presents a critical challenge in computer vision, demanding precise modeling of both persistent geometric structures and transient deformations Cai et al. (2022); Du et al. (2021); Fang et al. (2022); Kratimenos et al. (2024); Li et al. (2022). Unlike static environments, dynamic scenes exhibit heterogeneous motion patterns - rigid components maintain temporal consistency while deformable regions require high-frequency trajectory modeling Xu et al. (2024); Duan et al. (2024); Bae et al. (2024). This inherent complexity creates dual challenges: preserving spatial coherence across time-varying geometries and capturing transient deformation details without over-smoothing artifacts.

While Neural Radiance Fields (NeRF) Mildenhall et al. (2021); Chan et al. (2022); Yang et al. (2022); Park et al. (2021b); Martin-Brualla et al. (2021) revolutionized static scene modeling through continuous volumetric integration, their dynamic extensions Choe et al. (2023); Gao et al. (2021); Liang et al. (2023b); Liu et al. (2023); Wang et al. (2023); Barron et al. (2021); Fridovich-Keil et al. (2023) reveal critical limitations in handling temporal discontinuities, particularly the conflicting requirements for spatial fidelity versus temporal coherence arising from uniform spectrum allocation. Although explicit representations Barron et al. (2023); Cao & Johnson (2023); Tancik et al. (2022) improve efficiency through 4D spacetime factorization, their low-rank decomposition induces feature collision in overlapping regions. Recent 3D Gaussian Splatting (3DGS) Kerbl et al. (2023); Duisterhof et al. (2023); Yang et al. (2023); Liang et al. (2023a); Lin et al. (2024) has achieved impressive effects for static environments, where discrete volumetric primitives enable both photorealistic rendering and computationally efficient optimization through differentiable rasterization Shao et al. (2023); Uu et al. (2024); Lu et al. (2024); Luiten et al. (2024); Kratimenos et al. (2024).

However, their direct extension to dynamic scenarios faces three fundamental limitations (detailed theoretical analysis can be found in Appendix. E): 1) existing deformable methods suffer from either over-smoothing due to low-rank decomposition or feature collision from high-dimensional grid sampling, 2) previous Gaussian-based methods use a fixed threshold during Gaussian split stage which ignore adaptive split adjustment, and 3) persistent per-gaussian dynamics caused by intricate deformation are often neglected in current pipelines.

To address the challenges above, our key insight lies in addressing the anisotropic spatio-temporal sampling nature of dynamic scenes through hybrid explicit-implicit encoding. First, we develop a hybrid spectral-aware Laplacian motion flow extraction module that decouples spatial and temporal features into different frequency motion components, overcoming the feature collision of low-rank assumption while enabling adaptive frequency motion control. Then, we design an enhanced Gaussian dynamics attribute to perform individual Gaussian personalized dynamic optimization and design an adaptive regularization for identifying highly dynamic areas. Besides, we propose an adaptive Gaussian split strategy, which focuses on the optimization trade-off between Gaussian shape and anisotropy in dynamic scenes and an improved KDTree-based clustering algorithm was proposed to efficiently query and optimize dynamic Gaussians.

Our solution rethinks dynamic 3DGS through Laplacian spectral analysis, which provides a hybrid framework for localized frequency analysis. Meanwhile, we focus on the dynamics attribute of each Gaussian and the optimization problem in the derivation process, and propose a novel hybrid explicit-implicit algorithm model. In summary, our contributions are as follows:

- We propose a spectral-aware Laplacian Motion Flow Extraction module combining Hash encoding with Laplacian analysis that decouples different frequency motion trajectories from complex deformation.
- We design an enhanced Gaussian dynamics attribute that identify highly dynamic areas for adaptive split and regularization.
- We design an adaptive Gaussian split strategy that automatically adjusts the primitive density and anisotropy using KDTree-guided spectral analysis.

2 Related Work

2.1 NERF-BASED DYNAMIC MODELING

The advent of Neural Radiance Fields (NeRF) has significantly transformed the landscape of 3D scene reconstruction, particularly for static environments. However, extending NeRF to effectively model dynamic scenes remains a formidable challenge. Early works, such as D-NeRF Pumarola et al. (2021) and Nerfies Park et al. (2021a), have employed canonical space warping and temporal latent codes to capture motion. Despite their innovative approaches, these methods often exhibit limitations when dealing with rapid or abrupt movements. Moreover, explicit spacetime factorization techniques, such as HexPlane Cao & Johnson (2023), have been proposed to enhance computational efficiency. However, these methods impose restrictive low-rank assumptions that may oversimplify the intricate dynamics present in real-world scenes, particularly in environments characterized by rapid changes. Furthermore, while segmenting scenes into components with distinct attributes has

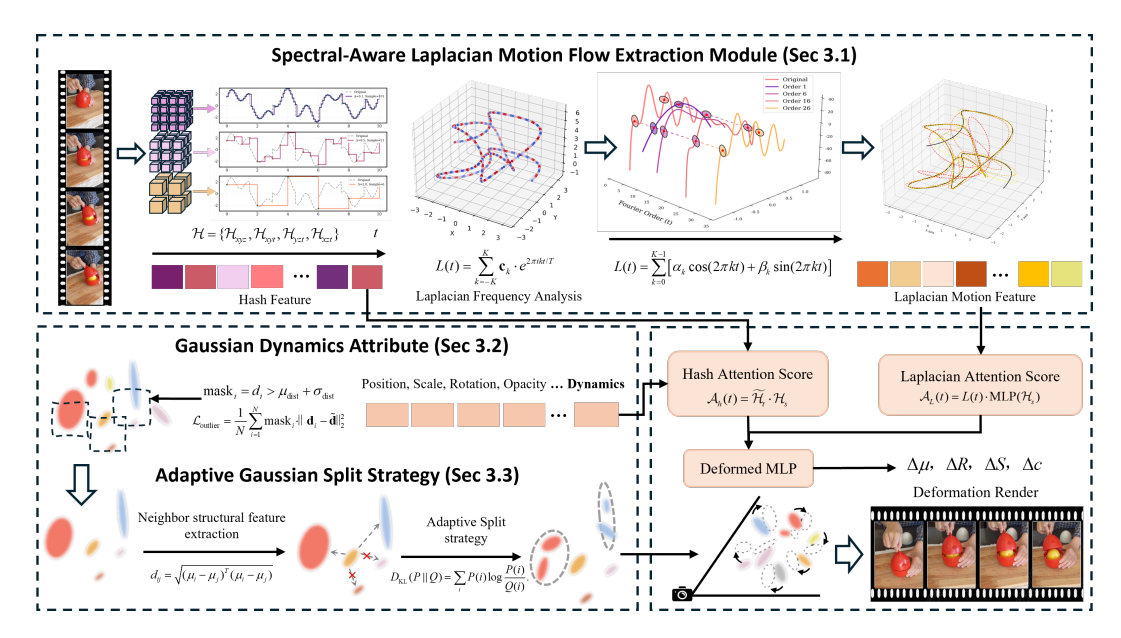


Figure 2: **Framework of our method.** We begin with a spectral-aware laplacian motion flow extraction module for motion trajectory tracking and adaptive frequency analysis. We design a Gaussian dynamic attribute with the spatio-temporal feature by attention mechanism. The whole pipeline benefits from the adaptive dynamic Gaussian split strategy for better performance and efficiency.

been explored to enhance modeling accuracy Gao et al. (2021); Tretschk et al. (2021), the implicit representations based on MLP often suffer from over-smoothing and lengthy training processes.

2.2 3DGS-BASED DYNAMIC MODELING

Recent advances in 3D Gaussian Splatting (3DGS) Kerbl et al. (2023); Yu et al. (2024); Huang et al. (2024); Li et al. (2024) have demonstrated remarkable success in static scene reconstruction, prompting extensions to dynamic scenarios. While 4D-GS Wu et al. (2024) employs multi-resolution Hex-Planes with MLPs for deformation modeling, it inherits the fundamental limitation of plane-based methods: the low-rank assumption leads to feature collisions and rendering artifacts in complex motions. Neural deformation fields Yang et al. (2024); Huang et al. (2024) address this through MLPs, but often produce over-smoothed results and struggle with high-frequency details due to insufficient inductive biases. Direct optimization of 4D Gaussians Yang et al. (2023); Duan et al. (2024) offers greater flexibility but introduces optimization challenges including floating artifacts and requires extensive training with additional regularizers. Grid4D Xu et al. (2024) has achieved impressive performance through combining triplane and Hash-coding while it often lacks smoothness and works without an explicit method for modeling dynamic processes. While SplineGS Park et al. (2024) proposes a pipeline that combine 3DGS and spline functions, however, it requires massive priors such as 2D trajactory and depth estimation to maintain performance. These limitations collectively highlight the need for a representation that balances expressiveness with efficient optimization for dynamic 3DGS, particularly in handling complex motions while preserving fine details. Our work addresses these limitations through a novel Laplacian motion flow extraction method that jointly optimizes for physical plausibility, computational efficiency, and multi-scale temporal fidelity.

3 METHODOLOGY

In this section, we present our methodology aimed at addressing the challenges of modeling 4D dynamic scenes with high-fidelity spatial details and complex temporal variations. The key innovation lies in a hybrid explicit-implicit representation that combines Laplacian analysis with spectral decomposition to capture spatial features and adaptive temporal dynamics. This framework is structured into three main components: spectral-aware Laplacian motion flow extraction module, enhanced Gaussian dynamic attribute and adaptive Gaussian split strategy. This hybrid approach is

designed to enhance the representation of motion dynamics while maintaining physical consistency across spatial and temporal domains, significantly outperforming existing methods in handling complex motion patterns. The overall pipeline is shown in Fig. 2.

3.1 Spectral-Aware Laplacian Motion Flow Extraction Module

This section focuses on the challenge of effectively encoding spatial and temporal information to capture the dynamics of motion. We employ a spectral-aware Laplacian motion flow extraction module that decomposes the frequency motion trajectories to accommodate the complexities of 4D spacetime. More theoretical analysis can be found in Appendix. E.

3.1.1 Multi-Scale Hash Encoding

To efficiently encode 4D spacetime information while preserving both spatial and temporal details, we employ a multi-scale hash encoding strategy that extends traditional methods. Inspired by Grid4D Xu et al. (2024), we extend InstantNGP's Hash encoding Müller et al. (2022) to 4D spacetime (x, y, z, t) through anisotropic multi-resolution decomposition.

$$\mathcal{H}^l = \{\mathcal{H}^l_{xuz}, \mathcal{H}^l_{xut}, \mathcal{H}^l_{uzt}, \mathcal{H}^l_{xzt}\}, \quad l \in \{1, ..., L\}$$

$$\tag{1}$$

Each level l maintains dimension-specific resolutions computed via geometric progression.

3.1.2 LAPLACIAN ANALYSIS FOR MOTION FLOW PREDICTION

For dynamic scene reconstruction, accurately predicting motion dynamics is paramount. Traditional methods often rely on MLP or linear interpolation, which fails to capture the complex periodic and aperiodic motions present in real-world dynamic scenes. To overcome these limitations, we propose a novel hybrid Laplacian motion flow representation that combines spectral analysis and learnable neural components, allowing for the effective capture of both low and high-frequency motion dynamics. The foundation lies in the Laplacian decomposition of time series:

$$L(t) = \sum_{k=-K}^{K} \mathbf{c}_k \cdot e^{2\pi i k t/T},$$
(2)

where L(t) represents the Laplacian motion field at time t, with \mathbf{c}_k denoting coefficients. Through Euler's formula, we substitute this representation into our motion prediction:

$$L(t) = \sum_{k=-K}^{K} \mathbf{c}_k \cdot \cos\left(\frac{2\pi kt}{T}\right) + i \sum_{k=-K}^{K} \mathbf{c}_k \cdot \sin\left(\frac{2\pi kt}{T}\right).$$
 (3)

This transformation naturally handles periodic motions common in dynamic scenes and the frequency components provide interpretable control over motion characteristics. To further enhance our motion representation, we extend the equation to a simple formulation:

$$L(t) = \sum_{k=0}^{K-1} \left[\alpha_k \cos(2\pi kt) + \beta_k \sin(2\pi kt) \right].$$
 (4)

Here, coefficients (α_k, β_k) are learnable parameters. This design aims to automatically adapt to scene-specific motion frequencies while maintaining end-to-end differentiability. The Laplacian decoding allows our model to learn appropriate frequency compositions directly from data space, eliminating the need for manual frequency band selection. The orthogonal basis properties enable stable gradient computation during optimization. Incorporation of learnable frequencies f_k through gradient enhances the ability to capture different frequency motion components:

$$\frac{\partial \mathcal{L}}{\partial f_k} = \frac{1}{\sigma_k^2} \sum_t \left(\frac{\partial \mathcal{L}}{\partial L(t)} \cdot t \cdot \left[-\alpha_k \sin(2\pi f_k t) + \beta_k \cos(2\pi f_k t) \right] \right),\tag{5}$$

where σ_k denotes temporal variance. This mechanism automatically balances frequency preservation with motion stability. Then we introduce an attention mechanism which combines Laplacian features with Hash spatial features \mathcal{H}_s :

,

$\mathcal{A}_L(t) = L(t) \cdot \text{MLP}(\mathcal{H}_s). \tag{6}$

3.1.3 MULTI-SCALE LAPLACIAN PYRAMID SUPERVISION

To enforce consistency across different frequency bands, we introduce a multi-scale supervision strategy that enforces consistency across frequency bands, enhancing the model's ability to better detail preservation. We supervise reconstruction using Laplacian pyramid decomposition:

$$\mathcal{L}_{lap} = \sum_{l=1}^{L} \lambda_l \|\mathcal{L}_l(I_{render}) - \mathcal{L}_l(I_{gt})\|_1, \tag{7}$$

where λ_l decreases exponentially to emphasize finer details. This loss function encourages model to focus on both coarse and fine features, ensuring a comprehensive understanding of motion dynamics.

3.2 ENHANCED GAUSSIAN DYNAMICS ATTRIBUTE WITH ADAPTIVE REGULARIZATION

To effectively model the dynamic variations inherent in complex scenes, we augment the standard 3D Gaussian Splatting representation. Specifically, we associate each 3D Gaussian G_i with a learnable dynamics attribute, denoted as $\mathbf{d}_i \in \mathbb{R}^{D_d}$, where D_d represents the dimensionality of this attribute space. The dynamics attribute \mathbf{d}_i is introduced to explicitly encapsulate these latent per-Gaussian conditional variations, providing a dedicated representation of dynamic properties.

To further improve the modeling of dynamic scene changes, we introduce a fusion mechanism that concatenates the original dynamic attribute vector \mathbf{d}_i with the Hash temporal feature \mathcal{H}_t , forming an augmented feature representation $\tilde{\mathcal{H}}_t = \text{Concatenate}(\mathbf{d}_i, \mathcal{H}_t)$.

This concatenation provides a straightforward yet effective means of integrating scene-specific temporal information with the Gaussian's intrinsic dynamic attributes, enabling the model to leverage both sources for more accurate deformation prediction. To effectively combine spatial and temporal information, we introduce an attention mechanism to aggregate spatio-temporal features through:

 $\mathcal{A}_h(t) = \tilde{\mathcal{H}}_t \cdot \mathcal{H}_s. \tag{8}$

3.2.1 Adaptive Dynamic Regularization

To ensure that our method better model dynamic changes, we implement a selective regularization mechanism that targets only those Gaussians exhibiting "abnormally large" or "highly dynamic" changes. These gaussians are referred to as "outliers", which need to be increase their gradients and thus promote their deformation or dynamic transformations.

Instead of using fixed thresholds or applying a regularization on all gaussians, our method employs a data-driven, adaptive dynamic selection scheme. Specifically, for each Gaussian, we compute the Euclidean distance between its dynamic attribute \mathbf{d}_i and a reference mean dynamic attribute $\bar{\mathbf{d}}_i$ as well as the associated standard deviation $d_i = \|\mathbf{d}_i - \bar{\mathbf{d}}\|_2$.

Let μ_{dist} and σ_{dist} denote the mean and standard deviation of all d_i across the Gaussian set. We then generate a mask to identify primitives that are significantly deviating from the normal scale:

$$\operatorname{mask}_{i} = d_{i} > \mu_{\operatorname{dist}} + \sigma_{\operatorname{dist}}. \tag{9}$$

Only the Gaussians satisfying this outlier criterion—i.e., those with $mask_i = 1$ —are subjected to the additional regularization loss:

$$\mathcal{L}_{\text{dy}} = \frac{1}{N} \sum_{i=1}^{N} \text{mask}_i \cdot d_i^2. \tag{10}$$

The purpose of this selective regularization is to intensify the gradients for Gaussians exhibiting large changes, thereby explicitly promoting their deformation and densification. By employing this dynamic regularization mechanism, the model adaptively concentrates regularization efforts on the most informative and dynamically relevant regions, effectively enhancing the capacity to model complex scene dynamics without imposing uniform constraints across all Gaussians.

In addition, we use Normalized cross-correlation (NCC) Yoo & Han (2009) loss \mathcal{L}_{NCC} to evaluate the similarity between two images while maintaining invariance to brightness variations to enhance alignment accuracy. The total loss \mathcal{L} used for training is made up of four distinct terms, each weighted by a corresponding hyperparameter λ to control its contribution:

$$\mathcal{L} = \mathcal{L}_{\text{orig}} + \lambda_{\text{NCC}} \mathcal{L}_{\text{NCC}} + \lambda_{\text{lap}} \mathcal{L}_{\text{lap}} + \lambda_{\text{dv}} \mathcal{L}_{\text{dv}}, \tag{11}$$

where \mathcal{L}_{orig} denotes original loss function of 3DGS and consists of \mathcal{L}_1 and Structural Similarity Index Measure (SSIM) loss functions Wang et al. (2004) \mathcal{L}_{SSIM} .

3.3 Adaptive Gaussian Split Strategy

In this section, we address the challenge of optimizing Gaussian representations of motion dynamics. Our approach utilizes the analysis about the structure of each Gaussian to adaptively refine Gaussian parameters based on local neighborhood information, enhancing the model's ability to capture complex motion patterns.

3.3.1 KDTREE-BASED PRIMITIVE ANALYSIS

To maintain spatial coherence and prevent overfitting, we analyze Gaussian primitives through their neighborhood relationships based on Euclidean distance. By examining the size and anisotropy of each Gaussian Xie et al. (2024), we can determine which Gaussians exhibit significant differences in their motion characteristics. Covariance differences are computed through L2 norm:

$$\Delta \Sigma_{ij} = \|\Sigma_i - \Sigma_j\|_2. \tag{12}$$

This adaptive approach ensures that our models remain responsive to local variations in motion dynamics. By focusing on Gaussians with notable differences in size and anisotropy, we can selectively choose which Gaussian to split, thereby enhancing the model's ability to represent complex motion patterns without introducing unnecessary complexity.

3.3.2 KL-DIVERGENCE GUIDED ADAPTATION

In some cases, we observed that the KDTree-based partitioning method can not accurately identify the dynamic Gaussian, which leads to the instability to capture dynamic motions. This is because the strategy of splitting Gaussian based on hard threshold will stop deriving when the shape and size of Gaussian in the neighborhood are similar. To further refine the Gaussian split process, we compute the KL-divergence between the neighbor Gaussian distribution P and a uniform distribution Q:

$$D_{KL}(P \parallel Q) = \sum_{k=1}^{K} P(k) \log \frac{P(k)}{Q(k)}$$
 (13)

The adaptive splitting threshold $\tau = \Delta \Sigma + D_{\text{KL}} \cdot \tau_{\text{base}}$, where τ_{base} is a hyperparameter. This mechanism allows for dynamic adjustments to the model complexity based on the observed motion patterns. Through adaptive dynamic Gaussian optimization strategy, we can determine when a Gaussian should be split more effectively, ensuring the model captures the nuances of motion dynamics while maintaining computational efficiency. This strategy enhances the robustness against overfitting by focusing on the most relevant Gaussian structures.

Table 1: Quantitative comparison to previous methods on HyperNeRF Park et al. (2021b) dataset. The higher $PSNR(\uparrow)$ and higher $SSIM(\uparrow)$ denote better rendering quality. The color of each cell shows the best and the second best.

Scene		broom2		v	rig-3dprint	er	,	vrig-chicke	n	vri	vrig-peel-banana		
Method	SSIM↑	PSNR↑	LPIPS↓	SSIM↑	PSNR↑	LPIPS↓	SSIM↑	PSNR↑	LPIPS↓	SSIM↑	PSNR↑	LPIPS↓	
HyperNeRF Park et al. (2021b)	0.210	19.51	_	0.635	20.04	_	0.828	27.46	_	0.719	22.15	_	
D3DGS Yang et al. (2024)	0.269	19.99	0.700	0.656	20.71	0.277	0.640	22.77	0.363	0.853	25.95	0.155	
MotionGS Zhu et al. (2024)	0.380	22.30	_	0.710	21.80	_	0.790	26.80	_	0.690	28.20	_	
MoDec-GS Kwak et al. (2025)	0.303	21.04	0.666	0.706	22.00	0.265	0.834	28.77	0.197	0.873	28.25	0.173	
4DGaussians Wu et al. (2024)	0.366	22.01	0.557	0.705	21.98	0.327	0.806	28.49	0.297	0.847	27.73	0.204	
ED3DGS Bae et al. (2024)	0.371	21.84	0.531	0.715	22.34	0.294	0.836	28.75	0.185	0.867	28.80	0.178	
Grid4D Xu et al. (2024)	0.414	21.78	0.423	0.723	22.33	0.245	0.848	29.27	0.199	0.875	28.44	0.167	
Ours	0.422	22.36	0.413	0.724	22.56	0.264	0.858	29.57	0.166	0.876	28.81	0.169	

Table 2: Quantitative comparison to previous methods on D-NeRF Pumarola et al. (2021) dataset. The color of each cell shows the best and the second best. More detail results can be found in supplementary material.

Method	SSIM↑	PSNR↑	LPIPS↓
3DGS Kerbl et al. (2023)	0.930	23.40	0.077
K-Planes Fridovich-Keil et al. (2023)	0.970	31.41	0.047
HexPlane Cao & Johnson (2023)	0.972	31.92	0.038
4DGaussians Wu et al. (2024)	0.985	35.32	0.021
D3DGS Yang et al. (2024)	0.991	40.08	0.013
SC-GS Huang et al. (2024)	0.993	41.66	0.009
Grid4D Xu et al. (2024)	0.994	41.99	0.008
Ours	0.994	42.17	0.007

4 Experiment

4.1 EXPERIMENT SETUP

We evaluate our method using three widely recognized datasets, comprising two real-world datasets and one synthetic dataset. The Neu3D Li et al. (2022) dataset is a real-world collection that features multiple static cameras and includes between 18 to 21 multi-view videos. We generate 300 frames for each video and initial point clouds for each scene following 4DGaussians Wu et al. (2024). HyperNeRF Park et al. (2021b) is a real-world dataset that captures continuous views with intricate topological variations at each timestamp within a dynamic scene. In our experiment, we utilized the "vrig" subset, which was captured using stereo cameras, training the model with data from one camera while validating it with data from the other. The D-NeRF Pumarola et al. (2021) dataset serves as a synthetic dataset tailored for monocular scenes, with each scene comprising between 50 to 200 frames. Due to discrepancies between the training and testing scenarios in the Lego subset of the D-NeRF Pumarola et al. (2021) dataset, we excluded it from our experimental analysis.

4.2 COMPARISONS

On the Neu3D dataset, our approach demonstrates exceptional proficiency as shown in Tab. 3. The primary challenge here lies in accurately modeling intricate, often non-rigid, temporal dynamics while simultaneously reconstructing high-fidelity static scene geometry from these fixed perspectives. Our method excels in generating temporally coherent motion representations and preserving sharp geometric details throughout the sequences, effectively disentangling dynamic elements from the static background. In contrast, competing methods frequently struggle to maintain long-term temporal consistency across the multiple views, often exhibiting noticeable motion blur, particularly during complex actions or over extended durations.

The HyperNeRF "vrig" subset introduces a distinct set of demanding conditions. This dataset tests the model's ability to handle complex motion while maintaining consistency across stereo viewpoints and adapt to evolving scene topology. Our method showcases remarkable resilience and adaptability in handling these extreme deformations and effectively leverages the stereo information, generalizing robustly across the viewpoints even when trained on one and validated on the



Figure 3: **Comparison Results.** Visual differences are highlighted with red insets for better clarity. Our approach consistently outperforms on D-NeRF Pumarola et al. (2021) dataset, demonstrating clear advantages in thin geometries and fine-scale details scenarios. Best viewed in color.

Table 3: Quantitative comparison to previous methods on Neu3D Li et al. (2022) dataset. Color of each cell shows the best and the second best. We show the average results of all scenes. More detail results can be found in supplementary material.

Method	SSIM↑	PSNR↑	LPIPS↓
4DGaussians Wu et al. (2024)	0.935	30.36	0.152
Grid4D Xu et al. (2024)	0.934	30.50	0.147
Spacetime Li et al. (2024)	0.944	31.46	0.142
ED3DGS Bae et al. (2024)	0.943	31.92	0.139
Ours	0.944	32.12	0.134

other as shown in Tab. 1 and Fig. 5. It consistently reconstructs intricate topological changes with greater accuracy and fewer visual artifacts or geometric distortions compared to existing approaches.

Furthermore, evaluation on the synthetic D-NeRF dataset underscores our method's inherent strength in inferring coherent 3D structure and plausible motion from limited input as shown in Tab. 2 and Fig. 3. Reconstructing dynamic 3D geometry from a single, potentially moving, camera viewpoint over time presents profound depth ambiguities and necessitates strong priors and temporal reasoning. Despite this inherent ill-posedness and the scarcity of explicit geometric cues, our approach generates remarkably temporally stable and geometrically plausible reconstructions. Consequently, it significantly outperforms baseline methods, which, under these monocular constraints, often exhibit pronounced depth inaccuracies that betray instabilities in their representation.

Across this diverse range of evaluated datasets, our method consistently achieves a marked superiority in performance. This advantage is evident in both the final reconstruction fidelity and the accurate, coherent capture of dynamic motion, ranging from subtle deformations to large-scale topological changes. This consistent success across varied and demanding conditions robustly validates the effectiveness, versatility, and broad applicability of our method for 4D reconstruction.

4.3 ABLATION STUDY AND ANALYSIS

To validate the effectiveness of each component within our framework, we conduct comprehensive ablation studies to validate the necessity of each component as shown in Tab. 4 and Fig. 4.

4.3.1 EFFECT OF LAPLACIAN MOTION FLOW EXTRACTION MODULE

Replacing this module with a defrom MLP leads to poorer performance, especially in scenes with diverse motion patterns or objects of varying sizes evolving over time. Dynamic scenes inherently possess variations across multiple spatial and temporal scales. This module is designed to capture these hierarchies effectively. It allows the model to represent fine details of motion trajectories while enabling the modeling of slow, gradual changes. By processing information hierarchically, it ensures consistent and accurate representation of scene dynamics across different frequency.

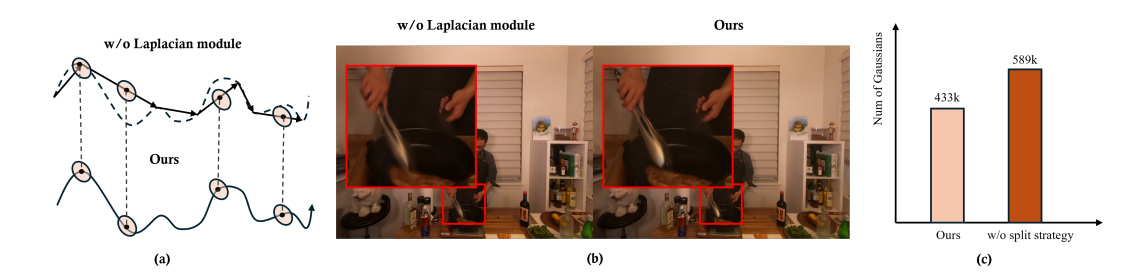


Figure 4: **Ablation Results.** Replacing Laplacian motion flow extraction module leads to poorer performance. Besides, the split strategy helps in reducing the number of final Gaussians.

Table 4: Ablation evaluation on Neu3D Li et al. (2022) dataset.

Method	SSIM↑	PSNR↑	LPIPS↓
w/o Laplacian module	0.938	31.64	0.149
w/o dynamic attribute	0.938	31.72	0.147
w/o adaptive split strategy	0.943	31.96	0.133
w/o $\mathcal{L}_{ ext{lap}}$	0.939	31.70	0.148
Ours	0.944	32.12	0.134

4.3.2 EFFECT OF ADAPTIVE GAUSSIAN SPLIT STRATEGY AND LAPLACIAN PYRAMID LOSS

Removing this component and reverting to original 3DGS split strategy results in a drop in reconstruction quality. This component improves render quality by intelligently allocating Gaussian primitives through densifying regions with high dynamics while pruning redundant primitives. This leads to a more compact representation of the scene and set of Gaussians compared to non-adaptive methods while achieving similar quality as shown in Tab. 4.

When this loss is removed on the rendered image, we observe a noticeable degradation in reconstruction quality. The Laplacian pyramid loss decomposes the reconstruction error across multiple frequency bands by comparing the Laplacian pyramids of the rendered and ground truth images. This loss function proves essential because it enforces structural consistency across different scales, effectively preserving fine details that would otherwise be lost in single-scale supervision.

4.3.3 EFFECT OF GAUSSIAN DYNAMICS ATTRIBUTE

Compared with full model, removing the Gaussian dynamics attribute leads to poorer performance. This difference underscores the importance of embedding dedicated dynamic attributes within the Gaussians themselves. By incorporating this, we allow each Gaussian to better adapt its shape and orientation according to its specific local dynamics, effectively capturing details and mitigating the feature collision issues inherent in relying solely on lower-rank grids.

5 Conclusion

In this paper, we present a novel approach for dynamic 3DGS that addresses the challenges of anisotropic spatio-temporal sampling through a hybrid explicit-implicit encoding framework. We introduced three key innovations: Firstly, a hybrid Laplacian motion flow extraction module combining Laplacian analysis with Hash encoding, effectively decoupling different motion frequencies from complex deformation details. Secondly, an enhanced Gaussian dynamics attribute that compensates for highly dynamic areas induced by geometric deformation. Thirdly, an adaptive Gaussian split strategy guided by KDTree-based analysis, which automatically adjusts dynamic primitive density and anisotropy. This work advance the state-of-the-art in dynamic scene modeling by bridging the gap between explicit representations and spectral analysis, with potential applications in VR/AR and scene reconstruction.

REFERENCES

- Jeongmin Bae, Seoha Kim, Youngsik Yun, Hahyun Lee, Gun Bang, and Youngjung Uh. Pergaussian embedding-based deformation for deformable 3d gaussian splatting. In *European Conference on Computer Vision*, pp. 321–335. Springer, 2024.
- Jonathan T Barron, Ben Mildenhall, Matthew Tancik, Peter Hedman, Ricardo Martin-Brualla, and Pratul P Srinivasan. Mip-nerf: A multiscale representation for anti-aliasing neural radiance fields. In *Proceedings of the IEEE/CVF international conference on computer vision*, pp. 5855–5864, 2021.
- Jonathan T Barron, Ben Mildenhall, et al. Zip-nerf: Anti-aliased grid-based neural radiance fields. In *Proceedings of the IEEE/CVF International Conference on Computer Vision*, pp. 19697–19705, 2023.
- Hongrui Cai, Wanquan Feng, Xuetao Feng, Yan Wang, and Juyong Zhang. Neural surface reconstruction of dynamic scenes with monocular rgb-d camera. Advances in Neural Information Processing Systems, 35:967–981, 2022.
- Ang Cao and Justin Johnson. Hexplane: A fast representation for dynamic scenes. In *Proceedings of the IEEE/CVF Conference on Computer Vision and Pattern Recognition*, pp. 130–141, 2023.
- Eric R Chan, Connor Z Lin, Matthew A Chan, Koki Nagano, Boxiao Pan, Shalini De Mello, Orazio Gallo, Leonidas J Guibas, Jonathan Tremblay, Sameh Khamis, et al. Efficient geometry-aware 3d generative adversarial networks. In *Proceedings of the IEEE/CVF conference on computer vision and pattern recognition*, pp. 16123–16133, 2022.
- Jaesung Choe, Christopher Choy, Jaesik Park, In So Kweon, and Anima Anandkumar. Spacetime surface regularization for neural dynamic scene reconstruction. In *Proceedings of the IEEE/CVF International Conference on Computer Vision*, pp. 17871–17881, 2023.
- Yilun Du, Yinan Zhang, Hong-Xing Yu, Joshua B Tenenbaum, and Jiajun Wu. Neural radiance flow for 4d view synthesis and video processing. In 2021 IEEE/CVF International Conference on Computer Vision (ICCV), pp. 14304–14314. IEEE Computer Society, 2021.
- Yuanxing Duan, Fangyin Wei, Qiyu Dai, Yuhang He, Wenzheng Chen, and Baoquan Chen. 4d gaussian splatting: Towards efficient novel view synthesis for dynamic scenes. *arXiv e-prints*, pp. arXiv–2402, 2024.
- Bardienus P Duisterhof, Zhao Mandi, Yunchao Yao, Jia-Wei Liu, Mike Zheng Shou, Shuran Song, and Jeffrey Ichnowski. Md-splatting: Learning metric deformation from 4d gaussians in highly deformable scenes. *arXiv preprint arXiv:2312.00583*, 2(3), 2023.
- Jiemin Fang, Taoran Yi, Xinggang Wang, Lingxi Xie, Xiaopeng Zhang, Wenyu Liu, Matthias Nießner, and Qi Tian. Fast dynamic radiance fields with time-aware neural voxels. In *SIGGRAPH Asia 2022 Conference Papers*, pp. 1–9, 2022.
- Sara Fridovich-Keil, Giacomo Meanti, Frederik Rahbæk Warburg, Benjamin Recht, and Angjoo Kanazawa. K-planes: Explicit radiance fields in space, time, and appearance. In *Proceedings of the IEEE/CVF Conference on Computer Vision and Pattern Recognition*, pp. 12479–12488, 2023.
- Chen Gao, Ayush Saraf, Johannes Kopf, and Jia-Bin Huang. Dynamic view synthesis from dynamic monocular video. In *Proceedings of the IEEE/CVF International Conference on Computer Vision*, pp. 5712–5721, 2021.
- Yi-Hua Huang, Yang-Tian Sun, Ziyi Yang, Xiaoyang Lyu, Yan-Pei Cao, and Xiaojuan Qi. Scgs: Sparse-controlled gaussian splatting for editable dynamic scenes. In *Proceedings of the IEEE/CVF conference on computer vision and pattern recognition*, pp. 4220–4230, 2024.
- Bernhard Kerbl, Georgios Kopanas, Thomas Leimkühler, and George Drettakis. 3d gaussian splatting for real-time radiance field rendering. *ACM Trans. Graph.*, 42(4):139–1, 2023.
- Agelos Kratimenos, Jiahui Lei, and Kostas Daniilidis. Dynmf: Neural motion factorization for real-time dynamic view synthesis with 3d gaussian splatting. In *European Conference on Computer Vision*, pp. 252–269. Springer, 2024.

- Sangwoon Kwak, Joonsoo Kim, Jun Young Jeong, Won-Sik Cheong, Jihyong Oh, and Munchurl Kim. Modec-gs: Global-to-local motion decomposition and temporal interval adjustment for compact dynamic 3d gaussian splatting. In *Proceedings of the IEEE/CVF Conference on Computer Vision and Pattern Recognition (CVPR)*, 2025.
 - Tianye Li, Mira Slavcheva, et al. Neural 3d video synthesis from multi-view video. In *Proceedings* of the IEEE/CVF conference on computer vision and pattern recognition, pp. 5521–5531, 2022.
 - Zhan Li, Zhang Chen, Zhong Li, and Yi Xu. Spacetime gaussian feature splatting for real-time dynamic view synthesis. In *Proceedings of the IEEE/CVF Conference on Computer Vision and Pattern Recognition*, pp. 8508–8520, 2024.
 - Yiqing Liang, Numair Khan, Zhengqin Li, Thu Nguyen-Phuoc, Douglas Lanman, James Tompkin, and Lei Xiao. Gaufre: Gaussian deformation fields for real-time dynamic novel view synthesis. *arXiv preprint arXiv:2312.11458*, 2023a.
 - Yiqing Liang, Eliot Laidlaw, et al. Semantic attention flow fields for monocular dynamic scene decomposition. In *Proceedings of the IEEE/CVF International Conference on Computer Vision*, pp. 21797–21806, 2023b.
 - Youtian Lin, Zuozhuo Dai, Siyu Zhu, and Yao Yao. Gaussian-flow: 4d reconstruction with dynamic 3d gaussian particle. In *Proceedings of the IEEE/CVF Conference on Computer Vision and Pattern Recognition*, pp. 21136–21145, 2024.
 - Yu-Lun Liu, Chen Gao, Andreas Meuleman, Hung-Yu Tseng, Ayush Saraf, Changil Kim, Yung-Yu Chuang, Johannes Kopf, and Jia-Bin Huang. Robust dynamic radiance fields. In *Proceedings of the IEEE/CVF Conference on Computer Vision and Pattern Recognition*, pp. 13–23, 2023.
 - Zhicheng Lu, Xiang Guo, Le Hui, Tianrui Chen, Min Yang, Xiao Tang, Feng Zhu, and Yuchao Dai. 3d geometry-aware deformable gaussian splatting for dynamic view synthesis. In *Proceedings of the IEEE/CVF Conference on Computer Vision and Pattern Recognition*, pp. 8900–8910, 2024.
 - Jonathon Luiten, Georgios Kopanas, Bastian Leibe, and Deva Ramanan. Dynamic 3d gaussians: Tracking by persistent dynamic view synthesis. In 2024 International Conference on 3D Vision (3DV), pp. 800–809. IEEE, 2024.
 - Ricardo Martin-Brualla, Noha Radwan, Mehdi SM Sajjadi, Jonathan T Barron, Alexey Dosovitskiy, and Daniel Duckworth. Nerf in the wild: Neural radiance fields for unconstrained photo collections. In *Proceedings of the IEEE/CVF conference on computer vision and pattern recognition*, pp. 7210–7219, 2021.
 - Ben Mildenhall, Pratul P Srinivasan, Matthew Tancik, Jonathan T Barron, Ravi Ramamoorthi, and Ren Ng. Nerf: Representing scenes as neural radiance fields for view synthesis. *Communications of the ACM*, 65(1):99–106, 2021.
 - Thomas Müller, Alex Evans, Christoph Schied, and Alexander Keller. Instant neural graphics primitives with a multiresolution hash encoding. *ACM transactions on graphics (TOG)*, 41(4):1–15, 2022.
 - Jongmin Park, Minh-Quan Viet Bui, Juan Luis Gonzalez Bello, Jaeho Moon, Jihyong Oh, and Munchurl Kim. Splinegs: Robust motion-adaptive spline for real-time dynamic 3d gaussians from monocular video. *arXiv preprint arXiv:2412.09982*, 2024.
 - Keunhong Park, Utkarsh Sinha, Jonathan T Barron, Sofien Bouaziz, Dan B Goldman, Steven M Seitz, and Ricardo Martin-Brualla. Nerfies: Deformable neural radiance fields. In *Proceedings of the IEEE/CVF international conference on computer vision*, pp. 5865–5874, 2021a.
 - Keunhong Park, Utkarsh Sinha, Peter Hedman, Jonathan T Barron, Sofien Bouaziz, Dan B Goldman, Ricardo Martin-Brualla, and Steven M Seitz. Hypernerf: A higher-dimensional representation for topologically varying neural radiance fields. *arXiv preprint arXiv:2106.13228*, 2021b.
 - Albert Pumarola, Enric Corona, Gerard Pons-Moll, and Francesc Moreno-Noguer. D-nerf: Neural radiance fields for dynamic scenes. In *Proceedings of the IEEE/CVF conference on computer vision and pattern recognition*, pp. 10318–10327, 2021.

- Johannes L Schonberger and Jan-Michael Frahm. Structure-from-motion revisited. In *Proceedings* of the IEEE conference on computer vision and pattern recognition, pp. 4104–4113, 2016.
- Johannes Lutz Schönberger, Enliang Zheng, Marc Pollefeys, and Jan-Michael Frahm. Pixelwise view selection for unstructured multi-view stereo. In *European Conference on Computer Vision (ECCV)*, 2016.
- Ruizhi Shao, Zerong Zheng, Hanzhang Tu, Boning Liu, Hongwen Zhang, and Yebin Liu. Tensor4d: Efficient neural 4d decomposition for high-fidelity dynamic reconstruction and rendering. In *Proceedings of the IEEE/CVF Conference on Computer Vision and Pattern Recognition*, pp. 16632–16642, 2023.
- Matthew Tancik, Vincent Casser, Xinchen Yan, Sabeek Pradhan, Ben Mildenhall, Pratul P Srinivasan, Jonathan T Barron, and Henrik Kretzschmar. Block-nerf: Scalable large scene neural view synthesis. In *Proceedings of the IEEE/CVF conference on computer vision and pattern recognition*, pp. 8248–8258, 2022.
- Edgar Tretschk, Ayush Tewari, et al. Non-rigid neural radiance fields: Reconstruction and novel view synthesis of a dynamic scene from monocular video. In *Proceedings of the IEEE/CVF International Conference on Computer Vision*, pp. 12959–12970, 2021.
- Chaoyang Wang, Lachlan Ewen MacDonald, Laszlo A Jeni, and Simon Lucey. Flow supervision for deformable nerf. In *Proceedings of the IEEE/CVF Conference on Computer Vision and Pattern Recognition*, pp. 21128–21137, 2023.
- Zhou Wang, Alan C Bovik, Hamid R Sheikh, and Eero P Simoncelli. Image quality assessment: from error visibility to structural similarity. *IEEE transactions on image processing*, 13(4):600–612, 2004.
- Guanjun Wu, Taoran Yi, Jiemin Fang, Lingxi Xie, Xiaopeng Zhang, Wei Wei, Wenyu Liu, Qi Tian, and Xinggang Wang. 4d gaussian splatting for real-time dynamic scene rendering. In *Proceedings of the IEEE/CVF conference on computer vision and pattern recognition*, pp. 20310–20320, 2024.
- Tianyi Xie, Zeshun Zong, et al. Physgaussian: Physics-integrated 3d gaussians for generative dynamics. In Proceedings of the IEEE/CVF Conference on Computer Vision and Pattern Recognition, pp. 4389–4398, 2024.
- Jiawei Xu, Zexin Fan, Jian Yang, and Jin Xie. Grid4d: 4d decomposed hash encoding for high-fidelity dynamic gaussian splatting. *arXiv preprint arXiv:2410.20815*, 2024.
- Gengshan Yang, Minh Vo, et al. Banmo: Building animatable 3d neural models from many casual videos. In *Proceedings of the IEEE/CVF Conference on Computer Vision and Pattern Recognition*, pp. 2863–2873, 2022.
- Zeyu Yang, Hongye Yang, Zijie Pan, and Li Zhang. Real-time photorealistic dynamic scene representation and rendering with 4d gaussian splatting. arXiv preprint arXiv:2310.10642, 2023.
- Ziyi Yang, Xinyu Gao, Wen Zhou, Shaohui Jiao, Yuqing Zhang, and Xiaogang Jin. Deformable 3d gaussians for high-fidelity monocular dynamic scene reconstruction. In *Proceedings of the IEEE/CVF conference on computer vision and pattern recognition*, pp. 20331–20341, 2024.
- Jae-Chern Yoo and Tae Hee Han. Fast normalized cross-correlation. *Circuits, systems and signal processing*, 28:819–843, 2009.
- Heng Yu, Joel Julin, Zoltán Á Milacski, Koichiro Niinuma, and László A Jeni. Cogs: Controllable gaussian splatting. In *Proceedings of the IEEE/CVF Conference on Computer Vision and Pattern Recognition*, pp. 21624–21633, 2024.
- Ruijie Zhu, Yanzhe Liang, Hanzhi Chang, Jiacheng Deng, Jiahao Lu, Wenfei Yang, Tianzhu Zhang, and Yongdong Zhang. Motiongs: Exploring explicit motion guidance for deformable 3d gaussian splatting. *Advances in Neural Information Processing Systems*, 37:101790–101817, 2024.

A ETHICS STATEMENT

This work adheres to the ICLR Code of Ethics. In this study, no human subjects or animal experimentation was involved. All datasets used were sourced in compliance with relevant usage guidelines, ensuring no violation of privacy. We have taken care to avoid any biases or discriminatory outcomes in our research process. No personally identifiable information was used, and no experiments were conducted that could raise privacy or security concerns. We are committed to maintaining transparency and integrity throughout the research process.

B REPRODUCIBILITY STATEMENT

We have made every effort to ensure that the results presented in this paper are reproducible. All code and datasets will be made publicly available after the paper is accepted to facilitate replication and verification. The experimental setup, including training steps, model configurations, and hardware details, is described in detail in the paper. We believe these measures will enable other researchers to reproduce our work and further advance the field.

C LLM USAGE STATEMENT

Large Language Models (LLMs) were used to aid in the writing and polishing of the manuscript. Specifically, we used an LLM to assist in refining the language, improving readability, and ensuring clarity in various sections of the paper. The model helped with tasks such as sentence rephrasing, grammar checking, and enhancing the overall flow of the text.

It is important to note that the LLM was not involved in the ideation, research methodology, or experimental design. All research concepts, ideas, and analyses were developed and conducted by the authors. The contributions of the LLM were solely focused on improving the linguistic quality of the paper, with no involvement in the scientific content or data analysis.

We have ensured that the LLM-generated text adheres to ethical guidelines and does not contribute to plagiarism or scientific misconduct.

D EXPERIMENTS SETTING DETAILS

Our framework is implemented on PyTorch and all experiments are conducted on a single RTX A6000 GPU. The scheduler of the learning rate primarily follows D3DGS Yang et al. (2024) and Grid4D Xu et al. (2024). Large Language Model (LLM) was employed to polish and refine the grammatical structure of this paper.

For training, we set the number of iterations to 30k for Neu3D Li et al. (2022), 30-40k for HyperNeRF Park et al. (2021b), 50k for D-NeRF Pumarola et al. (2021). The dimension resolution of the hash grids, the number of Laplacian coefficients, and the dimension of neighboring Gaussians used in the split strategy are adapted according to the scale of each scene. The Deformed MLP consists of a single-layer MLP with a width of 256, followed by a ReLU activation function. We implement 20 neighbors for dynamic regularization and configure the dynamic attribute with a dimension varying from 16 to 64 based on scenes, using a regularization coefficient of $\lambda_{\rm dy}=0.1$. The Laplacian-based loss is introduced starting from the 3k iteration, while the Normalized Cross-Correlation (NCC) loss Yoo & Han (2009) is applied from the 20k iteration onward. The loss weights are set to $\lambda_{\rm lap}=1$ and $\lambda_{\rm NCC}=0.01$ for common scene.

For D-NeRF Pumarola et al. (2021) dataset, the background is set to black, consistent with the settings in D3DGS Yang et al. (2024) and Grid4D Xu et al. (2024). For the scenes in the Neu3D Li et al. (2022), HyperNeRF Park et al. (2021b) dataset, we utilize the SFM Schonberger & Frahm (2016) points created from COLMAP Schönberger et al. (2016) to initialize Gaussians.

E THEORETICAL DERIVATION FOR LAPLACIAN MOTION FLOW EXTRACTION

We denote the dynamic motion field (per-point displacement) as a function over the 3D spatial domain and time:

$$\mathbf{u}(\mathbf{x},t) \in \mathbb{R}^3,\tag{14}$$

Stack per-Gaussian signals into a matrix/time series $U(t) = [\mathbf{u}_1(t), \dots, \mathbf{u}_N(t)]^{\top} \in \mathbb{R}^{N \times 3}$. For clarity, we treat one scalar channel and suppress the color and axis dimension.

E.1 LOW-RANK DECOMPOSITION

Assume we attempt to model the spatio-temporal field by a separable low-rank decomposition:

$$U(t) = PS(t) \approx \sum_{r=1}^{R} \mathbf{p}_r s_r(t), \tag{15}$$

where $P \in \mathbb{R}^{N \times R}$ and $S(t) \in \mathbb{R}^R$. This is equivalent to approximating each instantaneous spatial snapshot by an R-rank matrix. Any truncation to rank R eliminates singular vector directions with small singular values through SVD. Those small singular values often correspond to high spatial-frequency or localized deviations.

Let the per-time snapshot have spectral decomposition $U(t) = \sum_{k=1}^N \sigma_k(t) \mathbf{u}_k(t) \mathbf{v}_k^\top(t)$. Truncating to R keeps only $\sigma_1 \dots \sigma_R$. Because the energy of smooth, large-scale deformations concentrates in leading singular values, truncation discards small-energy but high-frequency components. Therefore, if approximating dynamics by low-rank temporal bases, the model cannot reconstruct rapid localized non-rigid motion that manifests as high-frequency components in either the spatial graph or temporal spectrum.

E.2 GRID SAMPLING AND HASH ENCODINGS

Consider encoding features on a discrete grid or hashed table over (x,y,z,t). The discrete sampling operator S maps a continuous field $u(\mathbf{x},t)$ to sampled values $u_s = S[u]$. According to Nyquist sampling theory, if the continuous field has frequency content above the sampling Nyquist limit, aliasing occurs and multiple different frequency components map to the same discrete samples.

The finite capacity of hash tables can cause different spatially close signals to map to similar indices, which acts like a low-pass operator in practice or unpredictable mixing of features. If the spacing of the sampling grid h is such that the maximum representable spatial frequency is $\omega_{\rm max}\approx\pi/h$, any true signal component with $|\omega|>\omega_{\rm max}$ will be observed as an aliased lower frequency ω_a satisfying $\omega_a=\omega-m\cdot(2\pi/h)$ for some integer m. That collapsed mapping between distinct frequencies is a collision in spectral domain caused by non-orthogonality between bases. High-dimensional encoding without spectral priors can produce inconsistent aliasing where different time frames map features to the same code.

Therefore, the low-rank or strong smoothing regularization enforces deformation consistency but attenuates the high frequencies. Conversely, high-capacity hash encodings can represent high frequencies, but without spectral regularization they produce inconsistent aliasing and feature collisions. We want to preserve high-frequency local motion details while maintaining smooth temporal coherence. We achieve this by decomposing the per-Gaussian signal into Laplacian eigenmodes.

E.3 LAPLACIAN EIGENBASIS

For Laplacian operator for graph structure or continuous field, we have:

$$\Delta f(x) = \nabla^2 f(x). \tag{16}$$

Eigenvectors u_k are orthonormal spatial modes ordered by increasing spatial frequency. Therefore, we can decompose the motion field into:

$$U(x,t) = \sum_{k} \alpha_k(t)\phi_k(x), \tag{17}$$

where α_k is obtained by Laplacian expansion $\alpha_k(t) = \sum_{m=-M}^M c_{k,m} e^{i2\pi mt/T}$ and the spatial basis $\phi_k(x)$ is orthogonal in L^2 space.

Laplacian gives an explicit spectral weighting, enabling us to optimize crucial frequency bands. Instead of hard low-rank truncation, spectral methods can preserve high-frequency coefficients at current time windows and penalize incoherent high frequencies across neighbors by shaping the penalty rather than an all-or-nothing rank truncation.

We use Laplacian spectrum expansion to model per-Gaussian dynamics. In this way, each dynamic attribute is decoupled into orthogonal components of different frequencies to ensure that it can express high-frequency details without interfering with each other in optimization.

F ADAPTIVE GAUSSIAN SPLIT STRATEGY DETAILS

We apply KL-divergence in split strategy by computing the KL-divergence between the neighbor Gaussian distribution P and a uniform distribution Q:

$$D_{KL}(P \parallel Q) = \sum_{k=1}^{K} P(k) \log \frac{P(k)}{Q(k)}.$$
 (18)

While the original notation used P and Q to suggest probability distributions, in our implementation they are instantiated as *zero-mean multivariate Gaussian distributions* with covariances Σ_i (for the candidate Gaussian) and $\bar{\Sigma}$ (mean of neighboring Gaussians), respectively. Specifically:

$$D_{KL}(N(0,\Sigma_i)||N(0,\bar{\Sigma})) = \frac{1}{2} \left[\operatorname{tr}(\bar{\Sigma}^{-1}\Sigma_i) - k + \log \frac{\det \bar{\Sigma}}{\det \Sigma_i} \right]. \tag{19}$$

To enhance stability and avoid directional bias, we adopt the symmetric KL divergence:

$$D_{KL} = D_{KL}(\Sigma_i \| \bar{\Sigma}) + D_{KL}(\bar{\Sigma} \| \Sigma_i). \tag{20}$$

The adaptive splitting threshold τ becomes:

$$\tau = \Delta \Sigma + D_{\text{KL}} \cdot \tau_{\text{base}}. \tag{21}$$

We set hyperparameter $\tau_{\rm base}=1e-4$. It serves as a scene-dependent parameter to determine when a candidate Gaussian significantly deviates from its local neighbors. A lower value allows more aggressive splitting in scenes with fine or deformable structures. To validate its effectiveness, we include an ablation in Tab. 5 to comparing results with different $\tau_{\rm base}$.

Table 5: The comparison results of different hyperparameter τ_{base} on D-NeRF datasets.

$ au_{\mathrm{base}}$	0			1e-2			1e-4	
Ours 0.994	PSNR	LPIPS	SSIM	PSNR	LPIPS	SSIM	PSNR	LPIPS
	42.07	0.008	0.994	42.01	0.008	0.994	42.17	0.007

G MORE EXPERIMENT RESULTS

In this section, more detail experiment results will be reported. Tab. 7, Tab. 8, Tab. 9 and Tab. 10 show the PSNR, SSIM and LPIPS results on dataset. Tab. 7 and Tab. 8 presents the detail results

 on Neu3D Li et al. (2022) dataset. Tab. 9 and Tab. 10 show the experiment results on the synthetic scenes of D-NeRF Pumarola et al. (2021) dataset. In addition, we add more rendering in Fig. 6 for HyperNeRF Park et al. (2021b) and Fig. 2 for Neu3D Li et al. (2022).

Our method demonstrates consistent superiority across all benchmarks, excelling where others struggle. On Neu3D (Tab. 7 and Fig. 2), our method adeptly handles complex temporal dynamics and reconstructs high-fidelity static geometry. It delivers temporally coherent motion, sharp details, and effective separation of dynamic and static elements, contrasting with competing approaches that often show motion blur, ghosting artifacts, or geometric distortions.

The HyperNeRF "vrig" subset (Fig. 6) show our strong adaptability to leverage stereo information for consistent reconstructions and generalization across views, with fewer visual artifacts and distortions than alternatives. For synthetic scene reconstruction on D-NeRF (Tab. 9 and Tab. 10), our method excels in inferring coherent 3D structures and motion from limited monocular inputs, overcoming depth ambiguities through robust temporal reasoning. This cross-dataset validation demonstrates that our framework uniquely combines geometric accuracy, temporal stability, and view consistency, validating its effectiveness and establishing state-of-the-art performance in dynamic scene reconstruction.

In addition, we provide detailed comparison with Grid4D Xu et al. (2024) on the D-NeRF dataset in Tab. 6, including model size, training time, and inference speed. As we can see, on the D-NeRF dataset, our model has 51MB, slightly larger than Grid4D (50MB). This size increase is due to our incorporation of Laplacian-based frequency modeling and dynamic appearance embedding, which offer improved flexibility and fidelity for dynamic scenes.

Moreover, our method requires about 2 hours per scene, which is a little longer than Grid4D (1h). Furthermore, our approach achieves 169 FPS at 800×800 resolution on D-NeRF scenes, enabling real-time rendering. While Grid4D reaches 180 FPS, it does not model dynamic attributes or frequency-aware motion. In contrast, our method achieves higher PSNR and better visual quality, offering a better quality-efficiency trade-off.

Table 6: Detailed comparison on D-NeRF datasets about model size, training time and the rendering FPS of our method.

	SSIM	PSNR	PSNR	Szie	Time	FPS
Grid4D	0.994	41.99	0.008	50MB	1h5min	180
Ours	0.994	42.17	0.007	51MB	2h6min	169

Table 7: Quantitative comparison to previous methods on Neu3D Li et al. (2022) dataset. The higher $PSNR(\uparrow)$ and higher $PSNR(\uparrow)$ denote better rendering quality. The color of each cell shows the best.

Scene	coffee_martini SSIM↑ PSNR↑ LPIPS↓				ook_spina PSNR↑		cut_roasted_beef SSIM↑ PSNR↑ LPIPS↓			
4DGaussians Wu et al. (2024) Grid4D Xu et al. (2024) Spacetime Li et al. (2024) ED3DGS Bae et al. (2024)	0.910 0.896 0.914 0.917	28.52 27.77 28.55 29.26	0.162 0.177 0.158 0.147	0.946 0.948 0.954 0.948	32.46 32.03 32.39 32.61	0.153 0.144 0.141 0.146	0.938 0.943 0.952 0.951	31.01 31.41 32.70 33.64	0.153 0.142 0.143 0.144	
Ours	0.918	29.60	0.147	0.952	32.74	0.133	0.954	33.37	0.132	

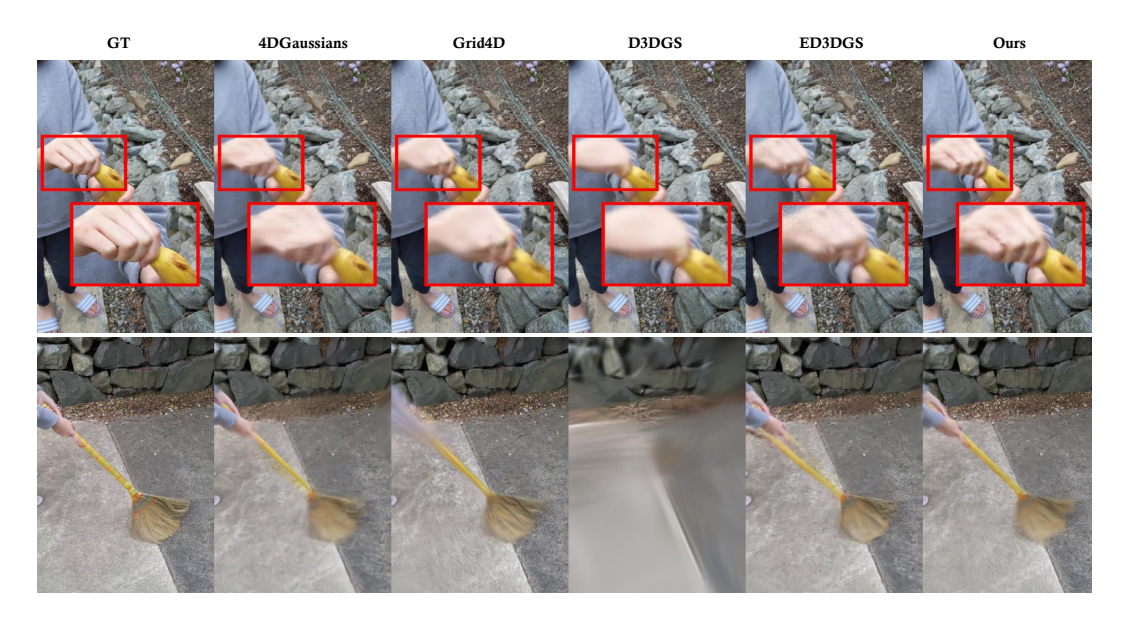


Figure 5: **Comparison Results.** Our approach consistently outperforms on HyperNeRF Park et al. (2021b) dataset, demonstrating advantages in challenging scenarios. Best viewed in color.

Table 8: Quantitative comparison to previous methods on Neu3D Li et al. (2022) dataset. The higher $PSNR(\uparrow)$ and higher $PSNR(\uparrow)$ denote better rendering quality. The color of each cell shows the best.

Scene	flai	me_salmo	n_1	l f	lame_stea	ık		sear_stea	k
	SSIM↑	$PSNR\!\!\uparrow$	$LPIPS\!\downarrow$	SSIM↑	$PSNR \!\!\uparrow$	$LPIPS\!\downarrow$	SSIM↑	PSNR↑	LPIPS↓
4DGaussians Wu et al. (2024)	0.913	29.33	0.159	0.946	29.40	0.146	0.954	31.42	0.136
Grid4D Xu et al. (2024)	0.911	29.24	0.159	0.952	30.10	0.132	0.957	32.47	0.131
Spacetime Li et al. (2024)	0.921	28.59	0.147	0.961	32.79	0.132	0.964	33.76	0.130
ED3DGS Bae et al. (2024)	0.926	29.96	0.134	0.957	32.53	0.128	0.958	33.47	0.131
Ours	0.921	30.00	0.137	0.958	33.12	0.124	0.958	33.89	0.132

Table 9: Quantitative comparison to previous methods on D-NeRF Pumarola et al. (2021) dataset. The higher $PSNR(\uparrow)$ and higher $SSIM(\uparrow)$ denote better rendering quality. The color of each cell shows the best and the second best.

Scene		ouncingba	lls		hellwarrio			hook		j	umpingjac	ks
Scelle	SSIM↑	PSNR↑	LPIPS↓	SSIM↑	PSNR↑	LPIPS↓	SSIM↑	PSNR↑	LPIPS↓	SSIM↑	PSNR↑	LPIPS↓
3DGS Kerbl et al. (2023)	0.959	23.20	0.060	0.916	29.89	0.106	0.888	21.71	0.103	0.930	20.64	0.083
K-Planes Fridovich-Keil et al. (2023)	0.993	40.05	0.032	0.952	24.58	0.082	0.949	28.12	0.066	0.971	31.11	0.047
HexPlane Cao & Johnson (2023)	0.992	40.36	0.031	0.944	24.30	0.073	0.955	28.26	0.052	0.974	31.74	0.036
4DGaussians Wu et al. (2024)	0.994	40.78	0.014	0.974	28.86	0.037	0.976	32.82	0.027	0.986	35.41	0.020
D3DGS Yang et al. (2024)	0.996	41.36	0.009	0.987	41.34	0.025	0.985	36.86	0.017	0.989	37.43	0.013
SC-GS Huang et al. (2024)	0.995	41.59	0.009	0.989	42.19	0.019	0.990	38.79	0.011	0.992	39.34	0.008
Grid4D Xu et al. (2024)	0.996	42.62	0.008	0.991	42.85	0.015	0.990	38.89	0.009	0.993	39.37	0.008
Ours	0.996	42.72	0.008	0.991	43.02	0.014	0.991	39.20	0.009	0.993	39.45	0.008

Table 10: Quantitative comparison to previous methods on D-NeRF Pumarola et al. (2021) dataset. The higher $PSNR(\uparrow)$ and higher $SSIM(\uparrow)$ denote better rendering quality. The color of each cell shows the best and the second best.

Scene		mutant			standup			trex			Average	
Scelle	SSIM↑	PSNR↑	$LPIPS\downarrow$	SSIM↑	PSNR↑	$LPIPS\downarrow$	SSIM↑	PSNR↑	LPIPS↓	SSIM↑	PSNR↑	$LPIPS\downarrow$
3DGS Kerbl et al. (2023)	0.934	24.53	0.058	0.930	21.91	0.079	0.954	21.93	0.049	0.930	23.40	0.077
K-Planes Fridovich-Keil et al. (2023)	0.971	32.50	0.036	0.979	33.10	0.031	0.974	30.43	0.034	0.970	31.41	0.047
HexPlane Cao & Johnson (2023)	0.982	33.66	0.028	0.983	34.12	0.019	0.976	31.01	0.028	0.972	31.92	0.038
4DGaussians Wu et al. (2024)	0.988	37.68	0.016	0.990	37.97	0.014	0.984	33.75	0.022	0.985	35.32	0.021
D3DGS Yang et al. (2024)	0.994	42.09	0.007	0.994	43.79	0.008	0.993	37.67	0.010	0.991	40.08	0.013
SC-GS Huang et al. (2024)	0.996	43.43	0.005	0.997	46.72	0.004	0.994	39.53	0.009	0.993	41.66	0.009
Grid4D Xu et al. (2024)	0.996	43.94	0.004	0.997	46.28	0.004	0.995	40.01	0.008	0.994	41.99	0.008
Ours	0.997	44.13	0.003	0.997	46.59	0.003	0.995	40.08	0.007	0.994	42.17	0.007

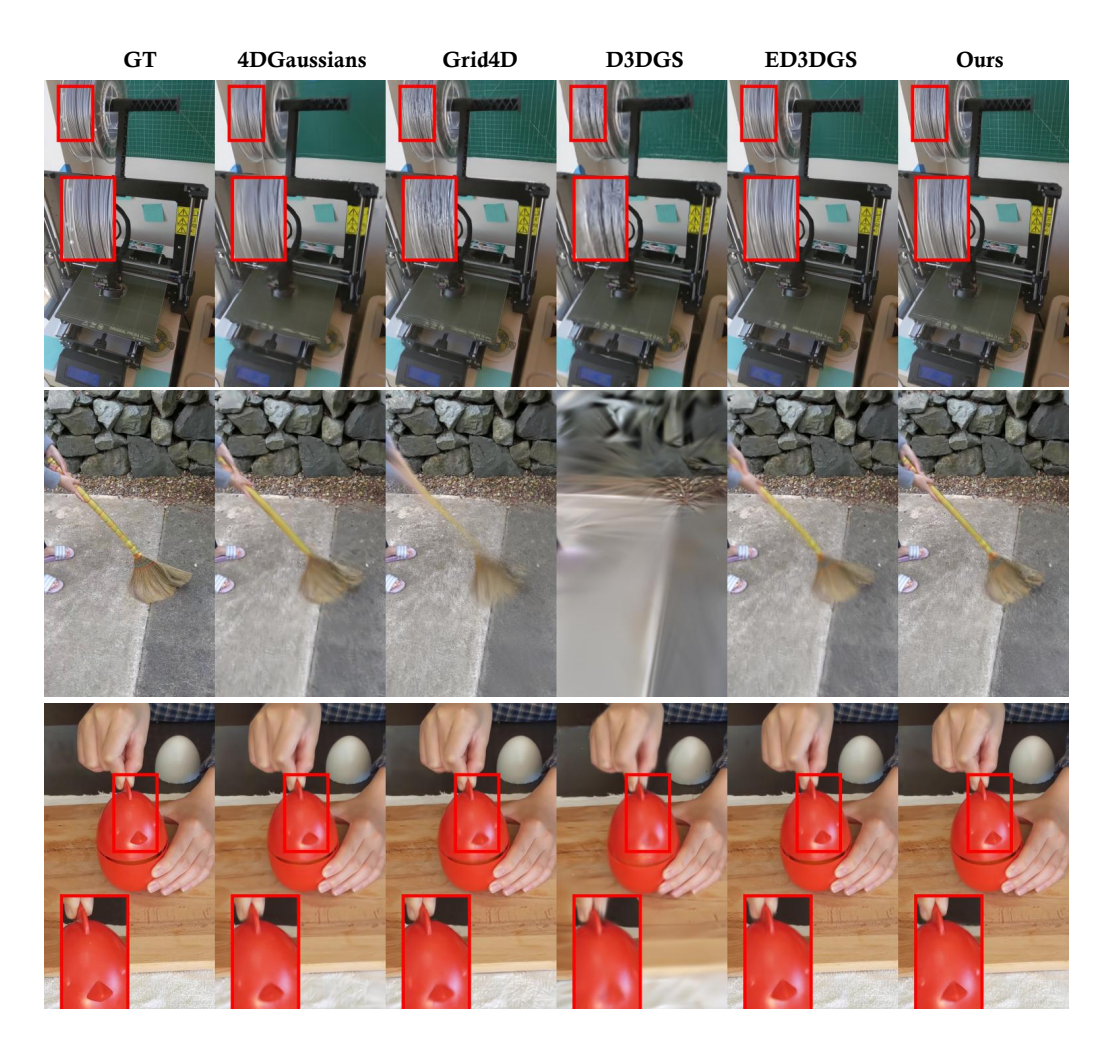


Figure 6: More Comparison Results on HyperNeRF Park et al. (2021b) dataset. Best viewed in color.



Figure 7: More Comparison Results on Neu3D Li et al. (2022) dataset. Best viewed in color.